

Article

Design and Validation of a Ten-Port Waveguide Reflectometer Sensor: Application to Efficiency Measurement and Optimization of Microwave-Heating Ovens

J.L. Pedreño-Molina^{1,*}, J. Monzó-Cabrera¹, A. Lozano-Guerrero¹ and A. Toledo-Moreo²

1 Departamento de Tecnologías de la Información y Comunicaciones, Universidad Politécnica de Cartagena / Campus Muralla del Mar s/n, 30202 Cartagena, Murcia, SPAIN

2 Departamento de Tecnología Electrónica, Universidad Politécnica de Cartagena / Campus Muralla del Mar s/n, 30202 Cartagena, Murcia, SPAIN

E-Mails: Juan.Pmolina@upct.es (J.L.P.); Juan.Monzo@upct.es (J.M.); Antonio.Lozano@upct.es (A.L); Ana.Toledo@upct.es (A.T)

* Author to whom correspondence should be addressed; Tel.: +34-968-326510; Fax: +34-968-325312

Received: / Accepted: / Published:

Abstract: This work presents the design, manufacturing process, calibration and validation of a new microwave ten-port waveguide reflectometer based on the use of neural networks. This low-cost novel device solves some of the previous reflectometer shortcomings such as non-linear behavior of power sensors, noise presence and the complexity of the calibration procedure, which is often based on complex mathematical equations. These problems, which imply the reduction of the reflection coefficient measurement accuracy, have been overcome by using a higher number of probes than usual six-port configurations and by means of the use of Radial Basis Function (RBF) neural networks in order to reduce the influence of noise and non-linear processes over the measurements. Additionally, this sensor can be reconfigured whenever some of the eight coaxial power detectors fail, still providing accurate values in real time. The ten-port performance has been compared against a high-cost measurement instrument such as a vector network analyzer and applied to the measurement and optimization of energy efficiency of microwave ovens, with good results.

Keywords: reflectometer; microwave sensor; scattering parameter; neural calibration.

1. Introduction

Microwave-heating applications are slowly increasing their importance due to the emergent necessities of food industry, sanitary sector, chemical and pharmaceutical engineering and polymer production, among others. Although this technology is mature and can offer several advantages such as reduction of processing times, usage of clean energy and the resulting reduction of atmospheric pollution, it has to compete against cheaper energies based on combustion to generate heat. Therefore, one of the main needs of microwave heating technology at industrial applications is the monitoring of energy efficiency in order to optimize its use and detect system malfunctions.

The power efficiency of a microwave oven can be easily related to the reflection coefficient at the feeding port. The conventional non-invasive measurement techniques for the reflection coefficient are often based on directional couplers that separate incident and reflected power within the waveguide. The comparison of both contributions allows the estimation of the magnitude and phase of the reflection coefficient. To measure the reflection coefficient, Vector Network Analyzers (VNAs) and Six-Port Reflectometers (SPRs) are by far the most widely used instruments. Calibration is an essential step to guarantee accurate measurements with them, since noise, the phase error introduced by the cables and non-linear behavior of detectors may lead to high error levels.

VNAs are very high precision instruments that can be used at laboratory stages but, due to their high price, they are very seldom used at industrial sites. Additionally, the VNA configuration does not allow handling high-power levels easily. Therefore, SPRs are often used and are the preferred sensors for monitoring the reflection coefficient both at high and low power levels. This SPR is particularly interesting thanks to the use of power detectors instead of mixers and directional couplers, thus providing simpler circuits when compared to VNA configurations.

Several techniques for calibration of SPRs have been previously published [1-3]. These studies consider aspects such as dynamic range and non-linearity of power measuring diodes [1, 2]. The most extended calibration technique is based on the use of four standard loads whose reflection coefficients are very precisely known [3]. With this technique, the numerical solution for calibration equations can be represented in the complex plane by means of three circles. The intersection of the circles provides the desired solution for the calibration process.

Due to inherent noise and other measurement errors, the intersection point of the circles is extended in practice to a less precise area and error minimization techniques must be used in order to reduce the influence of these errors. A new calibration method based on Fourier coefficients proximity for SPR parameters was presented in [4] in order to reduce the calibration uncertainty. A calibration method based on the use of phase shifters and attenuators was also proposed in [5]. In [6], the calibration method is based on the analytical description of the communication system behavior and the measurements performed when two signals with a slight frequency difference are connected to the reflectometer's inputs.

Several calibration techniques propose the characterization of the diode behavior in order to improve calibration and measurement performance [7, 8]. Some examples of linear approximations for diode response versus frequency and operation temperature can be found at [9, 10]. Other alternatives that use thermistors for temperature control and monitoring are described in [11].

Calibration methods based on artificial neural networks (ANNs) were proposed in [12, 13]. This approach is advantageous for permitting automatic calibration procedures, although ANNs require a large number of known standards for the network training. However, automatic reflection coefficients generators can be easily built. In fact, some recent works have shown that sample movement within microwave ovens may generate large variations for reflection coefficient at the feeding port [14] and that they can be used as low-cost impedance generators.

In this work, a new ten-port waveguide reflectometer based on low-cost power detectors is presented. Eight coaxial probes are inserted within the waveguide in order to sample the standing wave present at the waveguide and thus to estimate reflection coefficient. The device is analyzed with CST Microwave Studio electromagnetic (EM) commercial software in order to ensure monomode working conditions. The electronic design of the built power measuring circuits is shown. The calibration procedure, based in ANN learning techniques, is also described. The ten-port sensor has been built and validated by obtaining both magnitude and phase values of reflection coefficient and comparing them to VNA performance, using the Industrial, Scientific and Medical (ISM) 2.45 GHz frequency for demonstration purposes. Finally, as an example of application, this sensor has been used to measure and optimize the energy efficiency of a microwave oven. The optimization process is based on placing the sample at the optimal position within the microwave cavity. An example of this procedures is described in this paper.

2. Basic Theory and design principles for a ten-port reflectometer

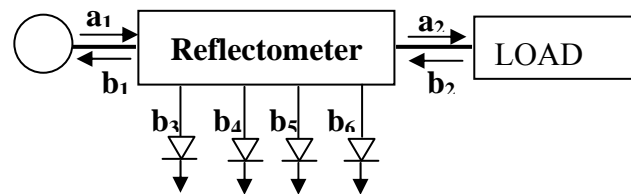
2.1. Six-port reflectometer review

A six-port reflectometer consists of a simple circuit with two ports for signal input and output, and four ports with their corresponding power detectors that sample the standing wave within the transmission line. The input port is connected to the EM source and the output port is connected to the load. This load can generate a mismatch that leads to reflections whose magnitude must be measured by the reflectometer.

Figure 1 shows a simplified scheme of a six-port reflectometer, where a_i signals go always into the i^{th} port and b_i signals go out from the i^{th} port. Ports ranging from 3 to 6 are supposed to be matched and therefore no reflected wave is considered there. In this scheme, Port 1 is the input port where the EM source is connected, whereas Port 2 is the output port of the sensor.

The complex reflection coefficient (Γ), also called S_{11} scattering parameter, provides a relationship between the incident wave amplitude at Port 1 (a_1) and the reflected wave amplitude (b_1) at the input port (Port 1 in Figure 1). The bigger the magnitude of Γ , the more energy is reflected to the EM source, thus less energy is absorbed by the load.

A numerical relationship can be obtained from power detected at Ports 3 to 6 to determine the reflection coefficient in the load. This numerical expression combines the value of nine complex parameters, very sensitive to measurement noise and non-linearities, in order to determine the desired reflection coefficient value.

Figure 1. Six-port reflectometer scheme.

The equation system shown in (1) relates the incident and reflected wave amplitudes at Port 2 to the sampling amplitudes. The calibration procedure of this six-port reflectometer is based on finding the numerical solution for this equation system, where M_i and N_i are complex constants. As described earlier, several calibration methods and load standards can be used.

$$\left. \begin{aligned} b_3 &= M_3 \cdot a_2 + N_3 \cdot b_2 \\ b_4 &= M_4 \cdot a_2 + N_4 \cdot b_2 \\ b_5 &= M_5 \cdot a_2 + N_5 \cdot b_2 \\ b_6 &= M_6 \cdot a_2 + N_6 \cdot b_2 \end{aligned} \right\} \quad (1)$$

To solve this system, eight linear equations must be considered. A theoretical linear dependence of all involved parameters could be obtained if noise, measurement perturbations and non-linear effects are not considered. However, the calibration procedure becomes a hard task under real conditions where the above mentioned effects can not be neglected.

Additionally, this configuration cannot be used when any of the power detectors is broken, damaged or saturated. This is due to the fact that the six-port uses the minimum amount of detecting ports that are required to find a precise solution. This may lead to delays both in laboratory measurements or industrial monitoring since the power detector must be repaired or changed, and then the whole device recalibrated, before being able to measure again.

2.2. Ten-port description

In this work a new ten-port reflectometer configuration is presented. In this case, a standard WR-340 waveguide section (4,3cm x 8,6 cm) has been used. Eight equally spaced coaxial probes have been inserted at the center of the wide wall of the waveguide. These coaxial probes sample the standing wave within the waveguide and therefore provide an estimation of the reflection coefficient. The output of these coaxial probes is connected to a non-linear low-cost power meter. Figure 2 shows the scheme of the proposed configuration where Ports 1 and 2 are respectively connected to the power source and load. Ports ranging from 3 to 10 correspond to the ports of coaxial probes.

The main advantage of this measurement configuration is that only a very small part of the delivered power is absorbed by the sampling probes, which allows that almost all the delivered power arrives to the sample. This is important mainly for high power applications such as microwave ovens, radar and etcetera. This structure is therefore different from that used by conventional laboratory equipment such as VNAs.

Figure 2. Ten port scheme with input and output ports and sampling coaxial ports, d being the distance between consecutive coaxial probes within the waveguide.

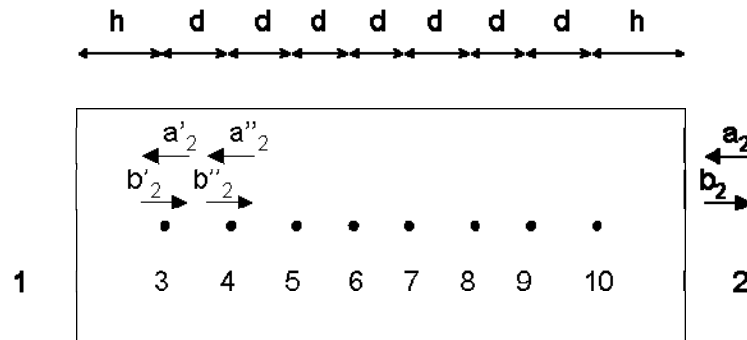
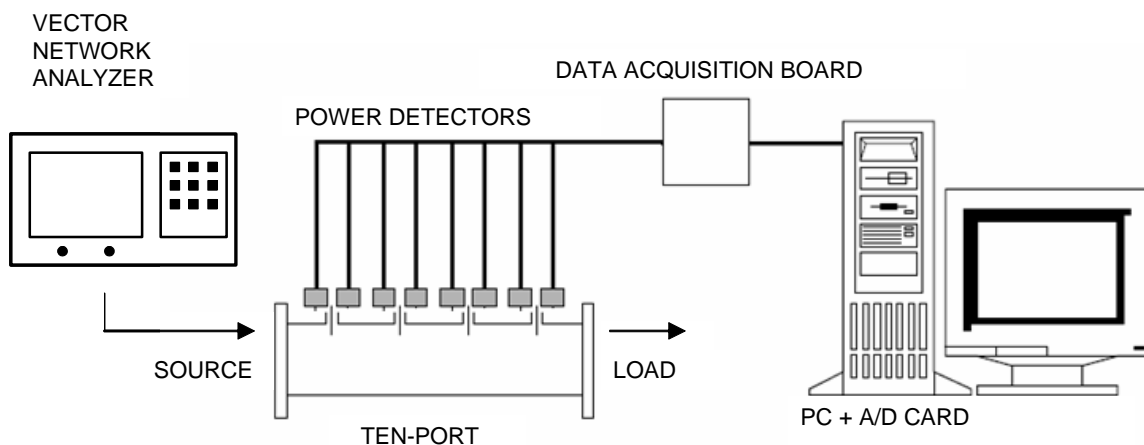


Figure 3 shows the complete measurement system diagram. As shown there, the power meters convert the radiofrequency power collected at the coaxial probes into a DC voltage. A personal computer and a data acquisition board are used in order to collect those voltages in real time. Additionally, a VNA is used at Port 1 in order to both generate the incident microwave power and to measure the reference value of the reflection coefficient for calibration purposes. A variable load is employed at Port 2 in order to generate changing values for the reflection coefficient at Port 1. Both the VNA reference measurements and the voltages at each coaxial probe are stored and subsequently processed by a RBF neural network in order to accomplish the calibration process. As a difference with previous works, no linearization process for the power meters is carried out, since this procedure is supposed to be inherently provided by the neural network calibration process.

Figure 3. Experimental measurement set up.



The measurement procedure is accomplished as follows:

- 1) The microwave source provides the incident wave (a_1) to the port.
- 2) The electromagnetic energy propagates along the waveguide reflectometer until it reaches the sample.
- 3) A reflected wave (b_2) is generated at the variable load thus generating a standing wave within the reflectometer.

- 4) The power sensors sample the energy of this microwave standing wave and convert the detected power into voltage in a logarithmic way.
- 5) Simultaneously, a VNA measures the reference value for the reflection coefficient.
- 6) These voltages obtained from power detectors and the reference reflection coefficient value are then introduced to a neural network. This neural network learns the relationship between the reference value of the reflection coefficient (output of the network) and the output voltages from power detectors (fed as inputs to the neural net).

2.3. Simulation of ten-port performance and design principles.

CST Microwave Studio electromagnetic commercial software has been used in order to test the performance of the ten-port reflectometer and to ensure that a monomode behavior is observed at Port 1, where the reflection coefficient is to be measured. In this case it is required that only the TE_{10} mode, which is the first propagating or fundamental mode of the rectangular waveguide, propagates along the ten-port. Equation (2) shows the cut-off frequency for both TE_{mn} and TM_{mn} modes in a rectangular waveguide:

$$f_{c_{mn}} = \frac{1}{2\sqrt{\mu_0\epsilon_0}} \sqrt{\left(\frac{m}{a}\right)^2 + \left(\frac{n}{b}\right)^2} \quad (2)$$

with $\mu_0=4\pi 10^{-7}$ H/m and $\epsilon_0=8.85 \times 10^{-12}$ F/m, being the vacuum magnetic permeability and electric permittivity, $a=8.6$ cm and $b=4.3$ cm the dimensions of the rectangular cross section of the waveguide and m and n the mode index that indicates the electric field maxima in each of the directions of the waveguide cross section. In our case, $f_{c10}= 1.74$ GHz for the considered dimensions of WR-340 waveguide. The cut-off frequency of higher modes such as TE_{01} and TE_{20} is $f_{c01}=f_{c20}=3.48$ GHz.

Since the proposed ten-port has been designed to work at 2.45 GHz and this frequency is higher than f_{c10} and lower than f_{c01} and f_{c20} , the TE_{10} mode is the only one allowed to propagate within the ten-port waveguide.

Figure 4 shows the electric field distribution of the TE_{10} mode. Figure 4.a) shows the electric field distribution at the cross-section perpendicular to the propagation direction and Figure 4.b) the distribution for this propagation direction. It can be observed that the maximum value for the electric field is located at the center of the waveguide and that the polarization of the electric field is oriented in the same way that the coaxial probes. Therefore, a good coupling is obtained between the sampling coaxial probes and the electric field.

Figure 5 shows the absolute value of the electric field along the waveguide. Although only one plane is shown, it should be born in mind that the electric field keeps constant along z direction, as shown in Figure 4.a). It can be observed that the introduction of metallic probes within the waveguide does not change the TE_{10} mode spatial distribution.

Figure 4. (a) Electric field distribution for TE_{10} mode at the waveguide perpendicular cross section. (b) Idem along the propagating direction.

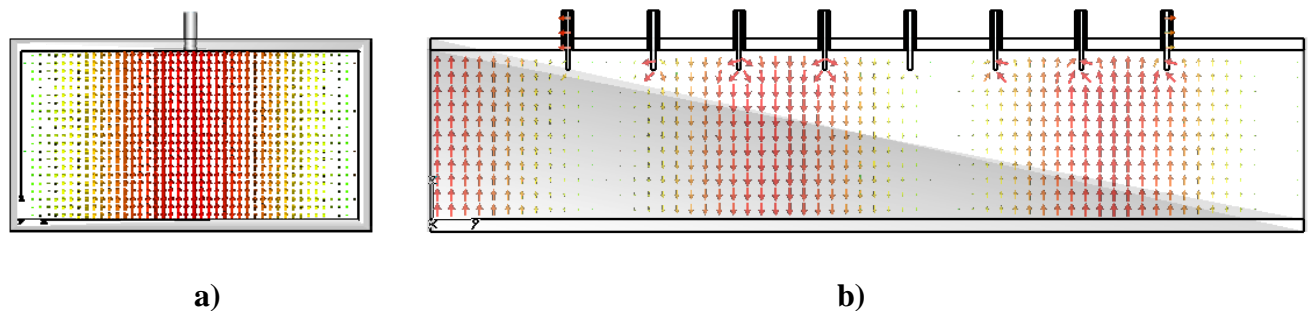
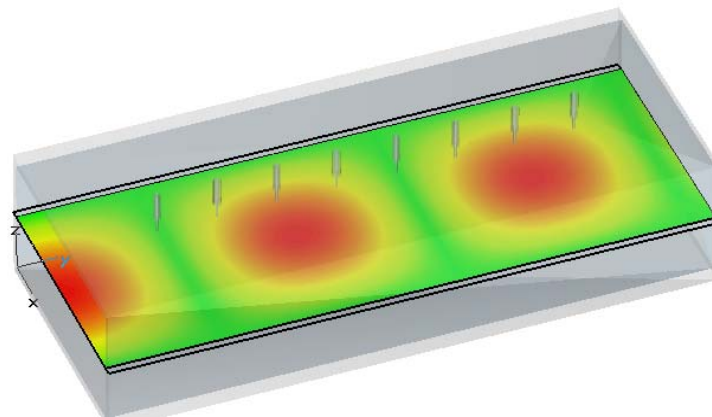


Figure 5. Electric field magnitude across a ten-port, including the effect of the metallic probes.



In order to specify the ten-port length, the TE_{10} waveguide length was calculated. In the WR-340 waveguide, this wavelength is 174.28 mm. Therefore, the ten-port length was fixed at 222.46 mm in order to contain at least this wavelength for the fundamental mode. Figure 6 shows the ten-port length and distances between probes. In Figure 7, a picture of the real implementation of the ten-port sensor in aluminum can be seen.

2.4. Power sensors and microstrip board circuits

Eight logarithmic power sensors have been employed for detecting both the magnitude and phase of the reflection coefficient. Each of the power detectors was associated to each of the coaxial ports. This number doubles the detectors employed in the six-port configuration in order to increase the amount of input data to the neural network and to reduce sampling distance of the standing wave when compared to the SPR configuration. This was supposed to reduce the error during the reflection coefficient estimation. In addition, this also permits the sensor to reconfigure whenever a detector fails, still providing accurate results, as it will be shown later.

Linear Technology LTC5530 (Schottky Diode RF Detector) power detectors were employed at each coaxial port. These detectors are non-linear and their working bandwidth covers from 300 MHz up to 7GHz. The input dynamic range allows power levels from -32 dBm to 10 dBm and the output DC-voltage range operates from 2.7V to 6V. Therefore, these power detectors transform the input radiofrequency power into a DC signal with a non-linear relationship.

It was necessary to include these integrated circuit power detectors within a microstrip board, in order to provide a coaxial to microstrip transition and to make available the necessary DC bias and ground for proper detector working. Microwave Office commercial software was employed to design the microstrip board. Figure 8 shows the corresponding schematic circuit and Figure 9 its layout. Circuit Cam software was used in order to manufacture the physical circuit.

Figure 6. Ten-port length and distances (in mm) between probes.

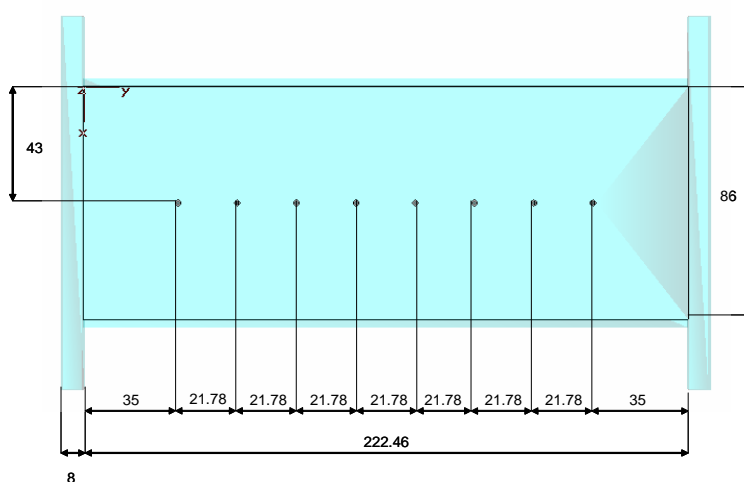


Figure 7. Real implementation of the ten-port reflectometer.



Figure 8. Schematic of the microstrip board for power detector use.

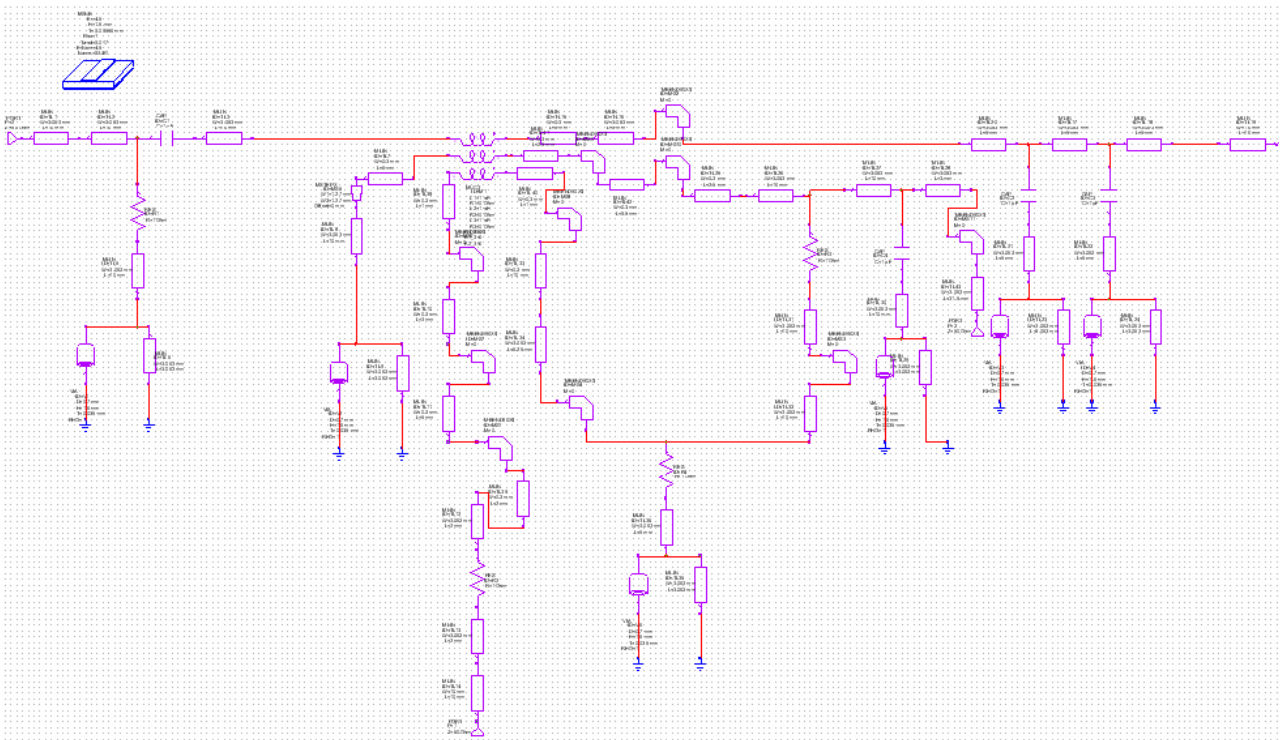
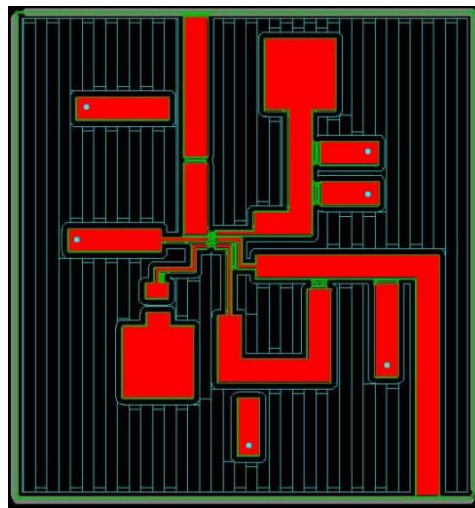


Figure 9. Layout of the microstrip board for power sensors.



2.5. Neural network for calibration

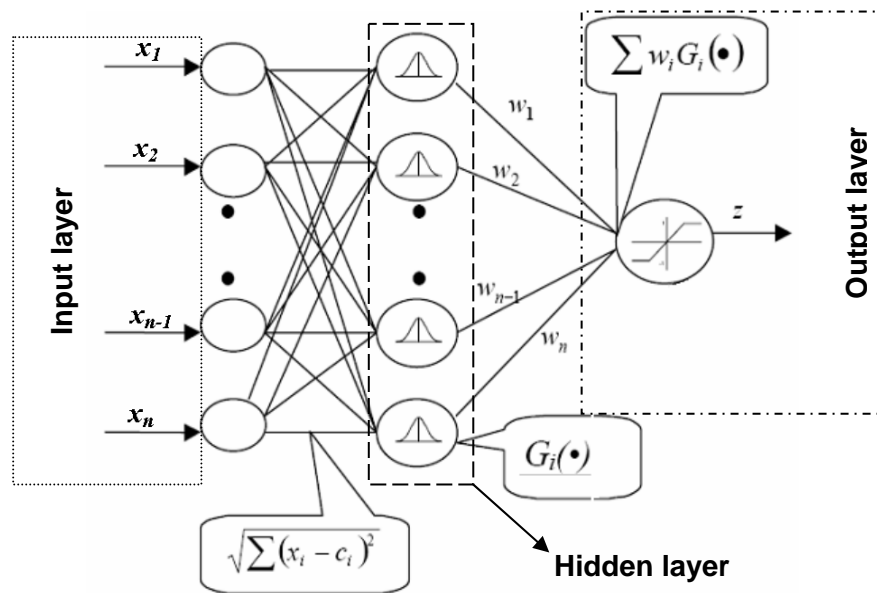
As described previously, conventional calibration of six-port reflectometers is based on the use of standard loads and several mathematical relationships which deal with complex numbers and that usually require optimization tasks to reduce the influence of measurement noise and power detectors non-linearity on final sensor accuracy. On the contrary, in this work we present a different calibration process based on the usage of neural networks to relate the DC voltage values provided by each power

detector to the reference reflection coefficient measurement. In this way, a ZVRE Rohde & Schwarz VNA was employed during the calibration procedure both for providing the 2.45 GHz incident signal at Port 1 and to measure the reference value of the reflection coefficient also at Port 1. The power level used both in calibration procedures and measurements was set to 0.5 watts.

A conventional RBF architecture has been used due to its simplicity. Figure 10 shows the structure of this kind of neural network. This neural architecture consists of a non-linear hidden layer and a linear output one, in which the contribution of the signals pondered by the G_i Gaussian activation functions of the neurons are combined to provide the S_{11} parameter at the working frequency. These functions are defined by the c_i adaptive centroids and a constant variance value for all the Gaussians.

The c_i centroids determine the segmentation of the input space of the \mathbf{x} input vector. The components x_i of vector \mathbf{x} are fed as inputs to the neural network. This input is processed by the Gaussians to give G_i , the output of the hidden level. The output of the network is obtained by means of the vectorial expression $\mathbf{W}\mathbf{x}\mathbf{G}$ in the output linear level, \mathbf{W} being the weights of the linear layer. In this case, the input vector is formed by the eight voltage values provided by the LTC5530 detectors, whereas the output of the network estimates $|S_{11}|$. A similar scheme is used for the estimation of S_{11} phase.

Figure 10. RBF neural network scheme.



RBFs are supervised neural networks whose structure provides a solution to the local interpolation of non-linear functions [15]. This is the case of the generic function $S_{11}(\mathbf{x})$, $\mathbf{x} = \{x_1, \dots, x_8\}$, considered in this work –see Figure 13– since it does not have a linear behaviour. Although the activation of the neurons in the RBF model is carried out by radial basis functions, this model has a linear expression for the estimation of S_{11} . Therefore, for each input vector $\mathbf{x}(k)$, the estimation of S_{11} is given by equations (3) and (4).

$$S_{11}(k) = \sum_{j=1}^M w_j G_j(k) \quad (3)$$

$$G_j(k) = \exp \left(- \frac{\sqrt{\sum_i (x_i(k) - c_j^i)^2}}{\sigma_j^2} \right) \quad (4)$$

where $G_j(k)$ is the output of the j^{th} Gaussian radial function at input $\mathbf{x}(k)$, c_j and σ_j are the centre and standard deviation of $G_j(k)$, w_j is the weight value associated to G_j , N is the number of examples used for training and M the number of neurons of the network.

The estimation of w_j is carried out by using the gradient descent algorithm to minimize the cost function described in Equation (5).

$$H = \sum_{k=0}^N \left(S_{11}^T(k) - S_{11}^M(k) \right)^2 \quad (5)$$

where $S_{11}^T(k)$ and $S_{11}^M(k)$ represent the theoretical and measured values for the parameter S_{11} , for both magnitude and phase.

As a conclusion, the application of the RBF neural network to the estimation of S_{11} permits to obtain, after the training stage, the optimal values for w_j . In the operation stage, the equation (3) supplies the approximation of $S_{11}(k)$ from DC voltages provided by power sensors.

3. Experimental set-up

Figure 11 shows the complete experimental set up implemented for the ten-port calibration and validation. A multimode 60 x 60 x 60 cm³ cavity has been employed for testing the sensor under real working conditions, and to provide different S_{11} values for calibration purposes. Two DC supply sources were employed for biasing the *LTC5530* power sensors. Power level of 0.5 watts was introduced by the ZVRE Rohde & Schwarz VNA at 2.45 GHz across Port 1. The neural network was implemented in a personal computer running MatlabTM Neural Network ToolboxTM routines. The personal computer was connected to the VNA by a USB GPIB communication board, and to the data acquisition board through conventional USB connectors. The error for RBF training was obtained by comparing the reference S_{11} value provided by the VNA and the value computed by the neural network as shown in Equation (3). This error was minimized when optimal w_j values were found after the optimization process.

Figure 12 shows the manufactured *LTC5530* circuit boards and common ground and biasing connections. The power-DC voltage conversion curve was measured by using the VNA as an RF signal generator, and a conventional multimeter for measuring the output voltage. This was needed since conversion curves were provided at 2 GHz but not at 2.45 GHz. Figure 13 shows the experimental determination of power voltage conversion curve at 2.45 GHz. This verified the correct implementation of power sensor boards.

Figure 11. Experimental set up for both sensor calibration and validation.

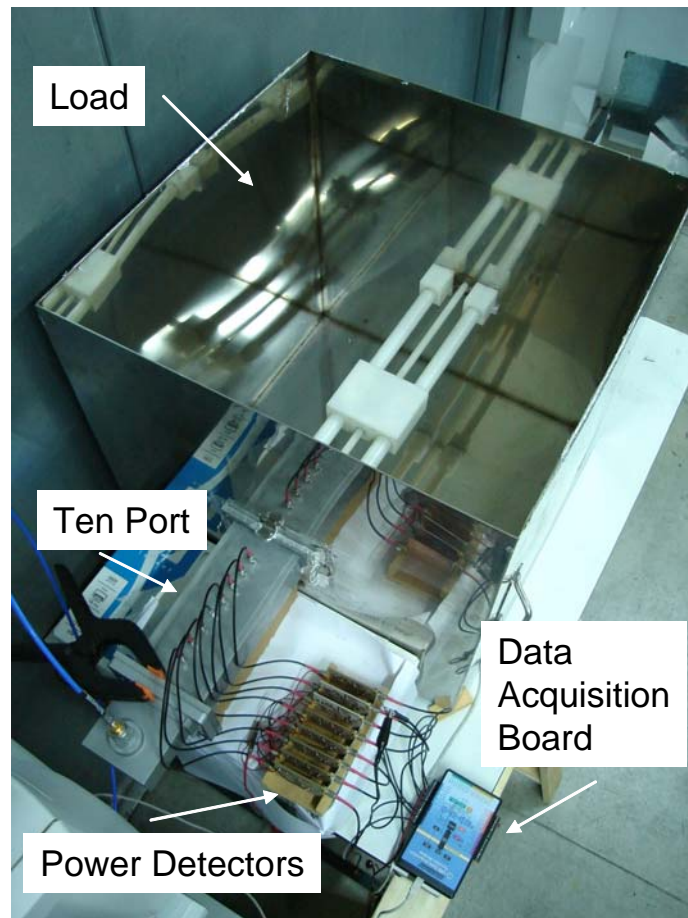


Figure 12. a) Manufactured power sensor boards. b) Rack disposition with biasing and ground connections.

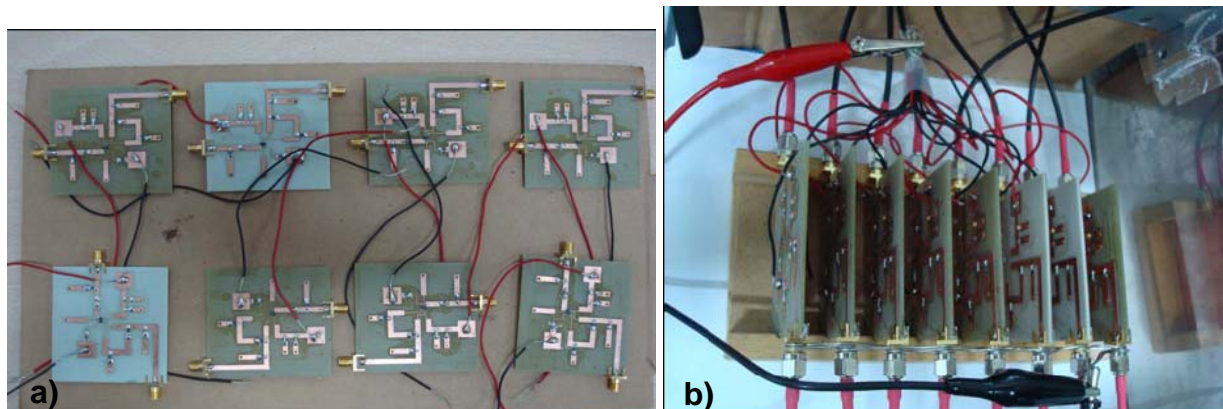
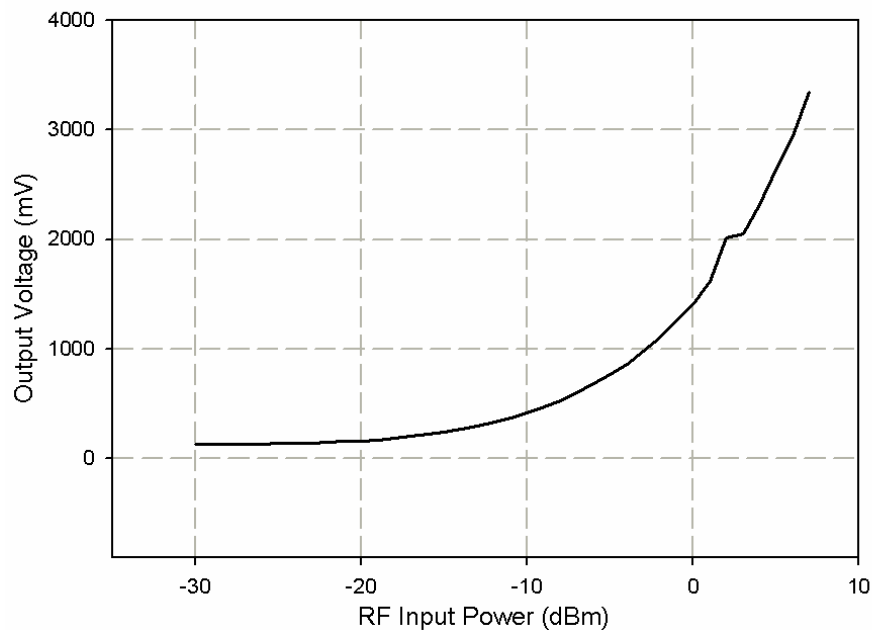


Figure 13. Obtained RF power-DC voltage conversion curve at 2.45 GHz.

Coaxial probes were designed to obtain a maximum input power level at the power sensor, equal to -10 dBm. The coupling of waveguide transmitted power in the coaxial probes was adjusted by changing the length of these coaxial probes within the waveguide. In this case, the coaxial probe coupling was adjusted to -17 dBm with a coaxial probe length equal to 16 mm.

During the calibration process, the RBF neural network was trained with $N=255$ training patterns. These patterns were formed by an input matrix with $N \times 8$ elements corresponding to the DC voltages from the power sensors and an output matrix with dimensions $N \times 2$, corresponding to the magnitude and phase of reference value of S_{11} provided by the VNA. A variable load provided different values for S_{11} . The phase and magnitude of training data for the S_{11} covered the ranges $[0, 2\pi]$ and $[0, 1]$, respectively. The number of Gaussian neurons was fixed to 60. The centers of the Gaussian neurons were chosen to be equally spaced, covering the whole range of the inputs. For all the neurons, σ_j was set to 0.3466.

4. Results and discussion

Figure 14 shows the training data for the S_{11} parameter provided by the VNA. These reference data are represented in the so called Smith chart that shows S_{11} both in magnitude and phase. Once the network has been trained, the weights of the RBF neural network are optimized and the sensor is ready to estimate the value of S_{11} only from power sensors' output values.

In this case, 74 patterns that had not been used during the training process have been employed for validation purposes. The S_{11} estimated values provided by the ten-port reflectometer have been compared to the ones measured by the VNA, both in magnitude and phase. Figure 15 shows the absolute error obtained for this comparison, obtaining an average absolute error of 6.2×10^{-3} for the magnitude and of 2.3×10^{-2} for the phase of S_{11} . As it can be observed in Figure 15, this error is very

small and therefore very accurate measurements can be made with the proposed reflectometer configuration. The phase error is bigger than the magnitude one, since phase can vary from 0 to 2π radians whereas magnitude variation ranges from 0 to 1.

Figure 14. Smith chart representation of S_{11} complex data used in the experimental training stage.

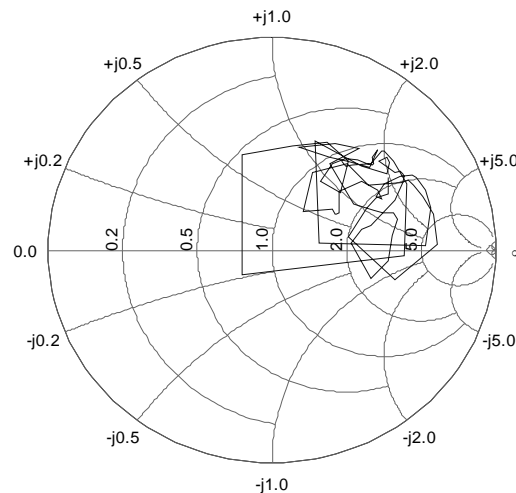
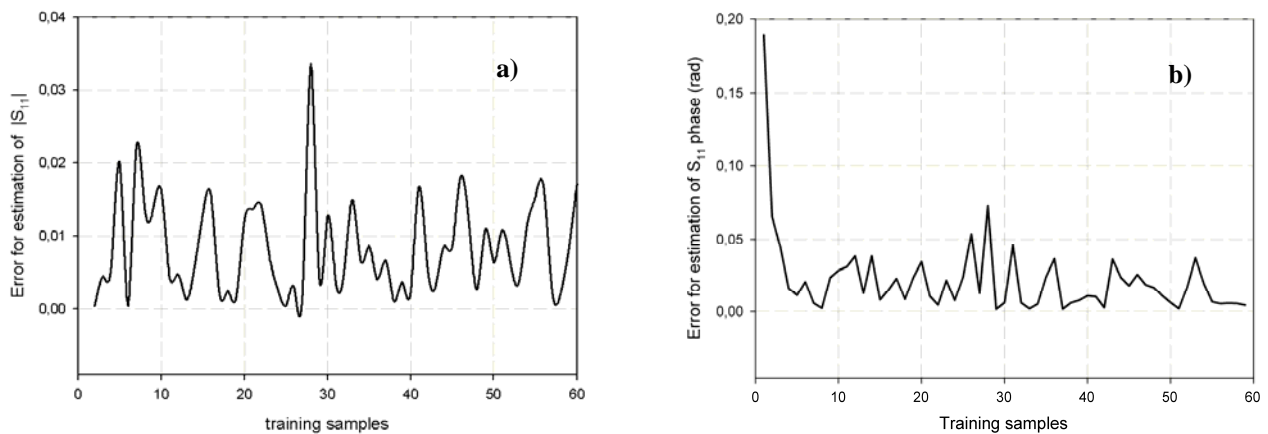


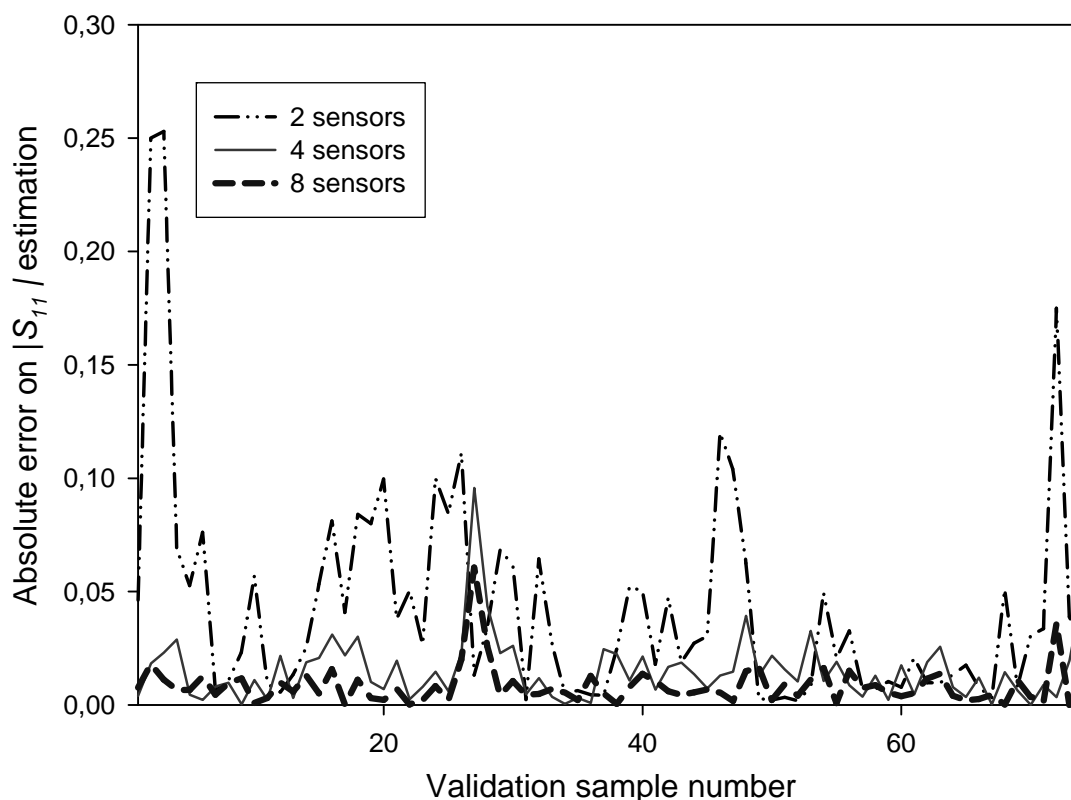
Figure 15. Validation error for 74 different validation patterns. (a) S_{11} magnitude. (b) S_{11} phase.



In order to evaluate the behaviour of the ten-port when some detectors are operating in an inaccurate way, several tests have been carried out by using only a reduced number of diodes as valid sensors to measure magnitude and phase for S_{11} . The output of the faulty detectors is defined as a constant value for all the training positions. The defective sensors were chosen in a random way. Some of the results obtained for the absolute error of $|S_{11}|$ when compared to VNA measurements are represented in Figure 16, where 255 training patterns and 74 validation measurements have been considered. From the curves in Figure 16, it can be observed that the proposed neural ten-port structure is able to correctly predict the S_{11} function even when some detectors are out of order. It is noticeable that the error observed when all the power sensors are working is lower than those obtained with 4

power sensors, which is the configuration of a conventional SPR. However, the error observed when only two power detectors are in use is not acceptable and a minimum of 4 power detectors should be used when carrying out the measurements. This is an expected result, as the Shannon theorem states that at least four samples along its wavelength are needed to correctly sample a wave without losing information. Therefore, these results show that it is possible to reconfigure the sensor software structure by training again the RBF neural network in order to correctly operate even when some of the power sensors are broken or faulty.

Figure 16. Robustness analysis. Behaviour of the reflectometer when different numbers of detectors are considered.



5. Sensor application to microwave oven optimization

Finally, as an application of the sensor capacities, the ten-port reflectometer has been used in order to optimize the behaviour of a $60 \times 60 \times 60 \text{ cm}^3$ microwave oven. The sensor was used to monitor the value of the S_{11} magnitude in real time for different positions of a 250 cm^3 cylindrical water sample. Figure 17 shows the scheme of the employed cavity. Optimization was carried out by properly placing the sample at the optimum position along the PTFE carrying system. Figure 18 shows the results obtained by the sensor for the S_{11} magnitude when 0.5 watts were employed as microwave power source and the sample was moved with the PTFE carrying system. The movement was carried out by

placing the sample as near as possible to the WR-340 coupling aperture and then moving the sample away from that position. As it can be observed at Figure 18, values lower than 0.2 can be obtained for S_{11} magnitude for sample distances around 46 cm away from the coupling aperture. On the contrary, other sample positions may lead to reflection coefficient values up to 0.75.

Therefore, the employment of this ten-port reflectometer allows, once it is calibrated, the monitoring of the reflection coefficient of microwave ovens in real time. It implies to improve the energy use and to protect the microwave sources from undesired reflections that may damage them.

Figure 17. Scheme of the multimode microwave oven employed during optimization process.

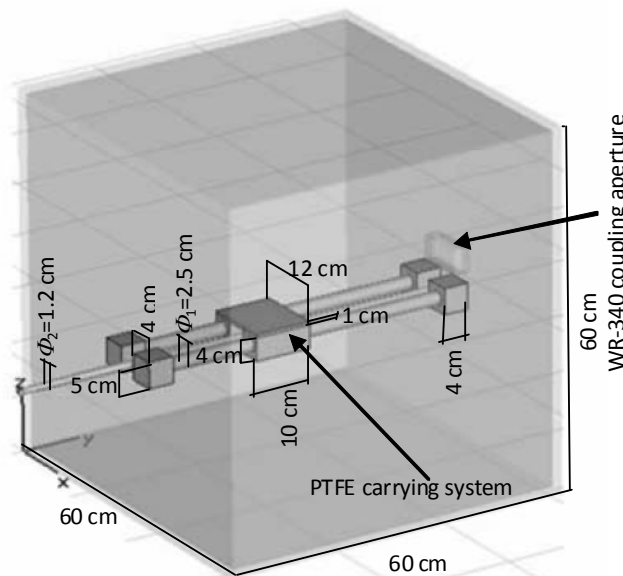
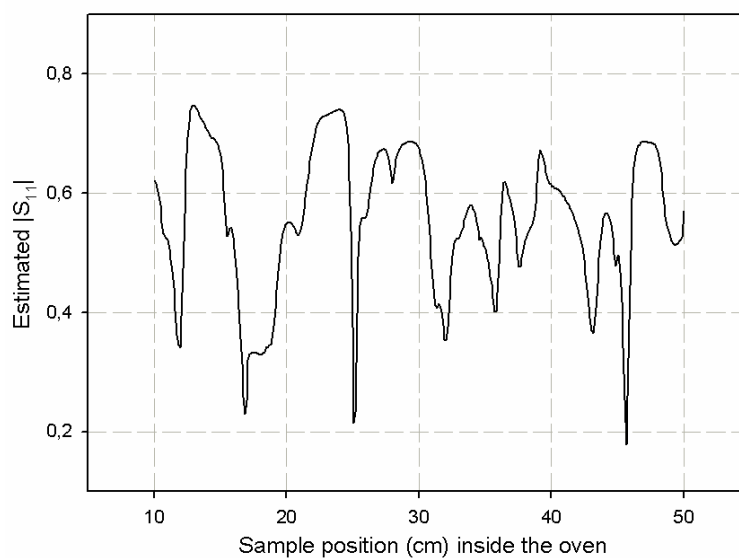


Figure 18. $|S_{11}|$ curve versus sample position within the multimode oven.



6. Conclusions

In this work the simulation, manufacturing and validation of a ten-port microwave sensor has been shown. This low-cost sensor allows the reflection coefficient estimation in real time and has been used in order to optimize microwave multimode ovens. The ten-port has been implemented in waveguide technology, which is the usual transmission medium used in power applications. A RBF neural network has been used to learn the relationship of power sensor output signals and the reference values of the reflection coefficient.

Experimental tests have shown that a very good estimation of the reflection coefficient can be obtained both for magnitude and phase, with accuracy comparable to high-cost laboratory equipment such as VNAs. Although results are shown for low power levels, the procedure can be readily extended to higher power levels by changing the coupling level of coaxial probes within the waveguide. An advantage shown by the sensor versus conventional waveguide reflectometers is that it can be readjusted even if some of the power detectors fail, still providing precise results. Additionally, linearization processes or theoretical modeling of the device are no longer needed for calibration, since neural networks learn and correct those problems by themselves.

References and Notes

1. Judah, S.R.; Holmes, W. A novel sixport calibration incorporating diode detector non-linearity. *IEEE Instrumentation and Measurement Technology Conference* **1998**, *1*, 592-595.
2. Moreau, J.; El Idrissi, A.; Tibaudou, C. Permittivity measurements of materials during heating by microwaves. *Meas. Sci. Technol.* **1994**, *5*, 996-1001.
3. Roussy, G.; Pearce, J.A. *Foundations and industrial applications of microwave and radio frequency fields: Physical and chemical processes*; John Wiley & Sons: West Sussex, UK, 1995.
4. Yakabe, T.; Kinoshita, M.; Yabe, H. Complete calibration of a six-port reflectometer with one sliding load and one short. *IEEE T. Microw. Theory* **1994**, *42*, 2035-2039.
5. Yakabe, T.; Ghannouchi, F.M.; Eid, E.E.; Fujii, K.; Yabe, H. Six-port self-calibration based on active loads synthesis. *IEEE T. Microw. Theory* **2002**, *50*, 1237-1239.
6. Rangel de Sousa, F.; Huyart, B.; de Lima, R.N. A new method for automatic calibration of 5-port reflectometers. *Journal of Microwaves and Optoelectronics* **2004**, *3*, 135-144.
7. Engen, G.F. Calibrating the six-port reflectometer by means of sliding terminations. *IEEE T. Microw. Theory* **1978**, *26*, 951-957.
8. Hoer, C.A. Performance of a dual six-port network analyzer. *IEEE T. Microw. Theory* **1979**, *27*, 993-998.
9. Wiedmann, F.; Huyart, B.; Bergeault, E.; Jallet, L. A new robust method for six-port reflectometer calibration. *IEEE T. Microw. Theory* **1999**, *48*, 927-931.
10. Wiedmann, F.; Huyart, B.; Bergeault, E.; Jallet, L. New structure for a six-port reflectometer in monolithic microwave integrated-circuit technology. *IEEE T. Microw. Theory* **1997**, *46*, 527-530.

11. Hesselbarth, J.; Wiedmann, F.; Huyart, B. Two new six-port reflectometers covering very large bandwidths. *IEEE T. Microw. Theory* **1997**, *46*, 966-969.
12. Liu, Y. Calibrating an industrial microwave six-port instrument using the artificial neural network technique. *IEEE T. Instrum. Meas.* **1996**, *45*, 651-656.
13. Pedreño-Molina, J.L.; Pinzolas-Prado, M.; Monzó-Cabrera, J. A new methodology for in-situ calibration of a neural network-based software sensor for S-parameter prediction in six-port reflectometers. *Neurocomputing* **2006**, *69*, 2451-2455.
14. Requena-Pérez, M.E.; Pedreño-Molina, J.L.; Monzó-Cabrera, J.; Díaz-Morcillo, A. Multimode cavity efficiency optimization by optimum load location: Experimental approach. *IEEE T. Microw. Theory* **2005**, *53*, 2838-2845.
15. Broomhead, D; Lowe, D. Multivariable functional interpolation and adaptive networks. *Complex Systems* **1988**, *2*, 322-355.

© 2008 by the authors; licensee Molecular Diversity Preservation International, Basel, Switzerland. This article is an open-access article distributed under the terms and conditions of the Creative Commons Attribution license (<http://creativecommons.org/licenses/by/3.0/>).